Improvements to the Dynamic Wake Meandering Model by incorporating the turbulent Schmidt number

Peter Brugger[1], Corey Markfort[2], and Fernando Porté-Agel[1]

[1]Wind Engineering and Renewable Energy Laboratory (WiRE), École Polytechnique Fedérale de Lausanne (EPFL), 1015 Lausanne, Switzerland

[2]IIHR-Hydroscience & Engineering, Dept. of Civil and Environmental Engineering, The University of Iowa, Iowa City, IA 52242, USA

Correspondence: Peter Brugger (peter.brugger@epfl.ch)

Abstract. Predictions of the dynamic wake meandering model (DWMM) were compared to flow measurements of a scanning Doppler lidar mounted on the nacelle of a utility-scale wind turbine. We observed that the wake meandering strength of the DWMM agrees better with the observation, if the incoming mean wind speed is used as advection velocity for the downstream transport, while a better temporal agreement is achieved with an advection velocity slower than the incoming mean wind speed.

5 A subsequent investigation of the lateral wake transport revealed differences to the passive tracer assumption of the DWMM in addition to a non-passive downstream transport reported in earlier studies. We propose to include the turbulent Schmidt number in the DWMM to improve (i) the consistency of the model physics and (ii) the prediction quality. Compared to the observations, the thus modified DWMM showed a root-mean-square error reduction by 2% for mean velocity deficit and 1% for the turbulence intensity, relative to the unmodified DWMM, in addition to better temporal agreement of the dynamics.

10 This is in contrast to an error increase of 35% and 36% if only a more accurate downstream transport velocity is used without including the turbulent Schmidt number.

1 Introduction

Wind turbine wakes impinging on other wind turbines within a wind farm are a significant source of power losses and they decrease the lifetime of affected wind turbines. Wake meandering is a low-frequency horizontal and vertical oscillation of the

15 entire wake (Taylor et al., 1985). Large-scale turbulence of the atmospheric boundary layer (Larsen et al., 2008) and bluff body vortex shedding (Medici and Alfredsson, 2006) have been proposed as drivers of wake meandering. Wake meandering affects power production due to its impact on the velocity deficit recovery, and it affects loads due to the turbulence added to the downstream flow (Larsen et al., 2013). Therefore, the modelling of wake meandering is one important aspect of wind farm development.

20 Modelling approaches for wake meandering can be grouped into two categories. The first group are computationally expensive large-eddy simulations (LES) that solve filtered flow equations at a high temporal and spatial resolutions (Mehta et al., 2014). However, their high fidelity comes at the cost of a time consuming forward integration and a difficult initialisation of the simulation. The second group are computationally inexpensive engineering models like the dynamic wake meandering model
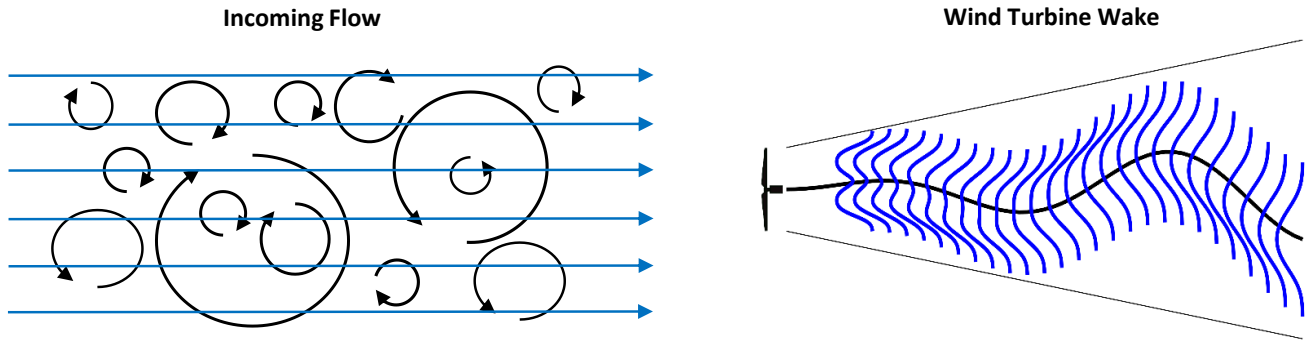
Figure 1. Illustration of wake meandering at an isolated wind turbine as assumed by the dynamic wake meandering model. Large-scale turbulence of the inflow displaces the wake of a wind turbine in the spanwise direction while it is transported downstream.

(DWMM) (Larsen et al., 2008) and a statistical modelling approach (Thøgersen et al., 2017). The DWMM is based on the
assumption that the wake behaves like a passive tracer, which is transported in the vertical and horizontal directions due to
large-scale turbulence without (Fig. 1). The DWMM has the advantage of fast computation time and it can be initialized with
measurement data that are commonly available at a wind farm.

The DWMM has seen validation efforts in literature, which are reviewed in the following. The underlying passive scalar
assumption of the DWMM has been accepted with the exception of the downstream transport velocity of wake meandering,
which is slower than the mean wind speed (Bingöl et al., 2010; Keck et al., 2014b; Machefaux et al., 2015; Conti et al.,
2021; Brugger et al., 2022). Machefaux et al. (2015) additionally investigated the lateral transport velocity of the wake while
it is meandering, but they had no measurements of the lateral velocity of the inflow for comparison. A validation of the
mean velocity field and turbulence intensity predicted by the DWMM against field measurements showed good agreement and
revealed a sensitivity to the eddy-viscosity parametrisation used (Reinwardt et al., 2018, 2020).

The above-mentioned discrepancies between the passive tracer assumption of the DWMM and observed transport behaviour
warrant closer examination. Specifically, assuming the wake as a passive tracer in the cross-stream directions and non-passive
in the streamwise direction is physically inconsistent. Also, an investigation of the impact of the downstream advection velocity
on the predictions of the DWMM has not been carried out so far. Further, previous validation efforts for the velocity deficit
and the turbulence intensity predicted by the DWMM focused on validating all components of the DWMM simultaneously,
with the exception of Reinwardt et al. (2020). Here, we extend the validation of the wake meandering module of the DWMM
by Reinwardt et al. (2020) to the turbulence intensity. This is especially interesting, because the meandering framework of the
DWMM is what sets it fundamentally apart from analytical wake models.

Therefore, this paper will compare the wake dynamics modelled by the DWMM to the wake dynamics observed with field
measurements. Further, we investigate how differences between modelled and observed wake meandering dynamics affect the
predictions of the DWMM for the effect of wake meandering on the mean velocity deficit and the turbulence intensity. These

research questions will be studied across a wide range of atmospheric conditions using field measurements of two pulsed Doppler LiDARs at a utility-scale wind turbine.

2 Methods

This section introduces first the DWMM (Sect. 2.1) followed by the research site and the instrument setup (Sect. 2.2) with which the data set for the model validation was collected (Sect. 2.3).

2.1 Dynamic wake meandering model

The dynamic wake meandering model (DWMM) was introduced by Larsen et al. (2007, 2008) and assumes the wake as a passive tracer that is advected by the large-scale turbulence of the atmospheric boundary layer. The model decomposes the wake into three parts: (i) a quasi-steady velocity deficit calculated with the thin shear layer approximation of the Naviar-Stokes equations (Ainslie, 1988), (ii) a wake meandering part modelled as a displacement of the entire wake with the large-scale turbulence of the background flow (Larsen et al., 2008), and (iii) small-scale turbulence based on a homogeneous Mann (1994) turbulence field that is scaled based on the local depth of the quasi-steady velocity deficit and its radial gradient. A schematic illustration of part (i) and (ii) is on the right of Fig. 1 with the quasi-steady velocity deficit in blue and the wake displacement in black. We follow here the implementation of Reinwardt et al. (2020) for the quasi-steady velocity deficit, including their recalibration, and Bingöl et al. (2010) for the wake meandering part. The small-scale turbulence part of the DWMM is not required here, because the present investigation focuses on the wake meandering part of the DWMM. The DWMM was implemented using the commercial software Matlab for this study.

2.1.1 Quasi-steady velocity deficit

The quasi-steady velocity deficit is modelled with the steady-state, axisymmetric thin shear layer approximation of the Naviar-Stokes equations with an eddy-viscosity turbulence closure (Ainslie, 1988). The momentum equation is given by

$$\overline{u}\frac{\partial \overline{u}}{\partial x} + \overline{v}_r \frac{\partial \overline{u}}{\partial r} = \frac{1}{r}\frac{\partial}{\partial r}\left(\nu r \frac{\partial \overline{u}}{\partial r}\right) \tag{1}$$

and the continuity equation is given by

$$\frac{1}{r}\frac{\partial}{\partial r}(r\overline{v}_r) + \frac{\partial \overline{u}}{\partial x} = 0, \tag{2}$$

where $\overline{u}$ is the mean wind speed in the axial direction, $\overline{v}_r$ is the mean wind speed in the radial (or spanwise) direction, r is the radial coordinate, x is the downstream coordinate, and ν is the eddy viscosity. The recalibrated mixing-length parametrisation of the eddy viscosity of Reinwardt et al. (2020) is given by

$$\frac{\nu}{\overline{u}_{hub}R} = k_1 F_1(\tilde{x})TI_u + k_2 F_2(\tilde{x})\max\left(\frac{R_w(\tilde{x})^2}{R\overline{u}_{hub}}\left|\frac{\partial U(\tilde{x})}{\partial r}\right|, \frac{R_w(\tilde{x})}{R}\left(1 - \frac{\overline{u}_{min}(\tilde{x})}{\overline{u}_{hub}}\right)\right), \tag{3}$$

where $\overline{u}_{hub}$ is the mean wind speed at hub height, $\overline{u}_{min}$ is the minimum velocity of the wake, TI_u is the longitudinal turbulence intensity at hub height, $\tilde{x} = x/R$, R is the rotor radius, R_w is the wake width, $k_1 = 0.0914$ and $k_2 = 0.0216$ are calibration constants, and F_1 and F_2 are empirical filter functions given by

$$F_1 = \begin{cases} 0.25\tilde{x}, & \text{for } \tilde{x} < 4, \\ 1, & \text{for } \tilde{x} \geq 4, \end{cases} \tag{4}$$

and

$$F_2 = \begin{cases} 0.035, & \text{for } \tilde{x} < 4, \\ 1 - 0.965 \exp\left(-0.35(0.5\tilde{x} - 2)\right), & \text{for } \tilde{x} \geq 4. \end{cases} \tag{5}$$

The system of partial differential equations given by Eq. (1) and Eq. (2) was solved on an isotropic grid with a resolution of $0.01D$ spanning $10D$ from the origin at the nacelle using the method of Crank and Nicolson (1947). The inner boundary condition is $V(r = 0) = 0$, and the outer boundary condition is $U(r = 10D) = u_{hub}$. The initial condition at $x = 0$ is introduced in the next section.

2.1.2 Initial velocity deficit at the rotor plane

The thin shear layer equations (Eq. 1 and Eq. 2) omit the pressure gradient terms. The effect of the pressure gradients is considered negligible at a distance of $3D$ (Madsen et al., 2010). Therefore, the boundary condition at $x = 0$ is designed to account for the effect of the neglected pressure gradient by including expansion and deceleration of the flow at the rotor disc such that the resulting flow field after $3D$ is accurately represented. The initial velocity deficit is iteratively given by

$$\overline{u}_{ini}(r_{w,i}) = \overline{u}_{hub}(1 - (1 + f_u)\overline{a}) \tag{6}$$

and

$$r_{w,i} = r_i \sqrt{\frac{1 - \overline{a}}{1 - (1 + f_R)\overline{a}}} \tag{7}$$

with $f_u = 1.1$, $f_R = 0.98$, $\overline{a}$ is the induction factor averaged along all radial positions, r_i is the rotor radius at position i, and $r_{w,i}$ is the wake radius at position i (Keck et al., 2013). The induction factor is computed from the thrust coefficient of the wind turbine (C_T) by using the relationship

$$C_T = 4\overline{a}(1 - \overline{a}), \tag{8}$$

where $\overline{a}$ is assumed to be constant across the rotor area. The thrust coefficient is selected from Fig A1 based on u_{hub}. The assumption of a constant induction factor is necessary because its radial distribution is not available to us for the wind turbine at the research site. However, testing with two different induction factor distributions of model wind turbines shown in literature (scaled so that they yield the same mean induction factor) showed that the two initial velocity deficits at $x > 4D$ had a mean absolute difference of 0.9% with a maximum of 1.5% based on the mean wind speed for the wind speed range covered in the results.

2.1.3 Wake meandering

The DWMM uses the hypothesis that the wake can be modelled as a passive tracer that is transported by the large-scale turbulence structures of the atmospheric boundary layer. The process can be imagined as a continuous sequence of velocity deficits emitted by the wind turbine that are passively transported by the large-scale turbulence (Larsen et al., 2008). Therefore, a suitable description of the turbulence field is required. We depart here from the implementation of Reinwardt et al. (2020), who used a Kaimal spectrum to generate a stochastic turbulence field, and instead we will follow the approach of Bingöl et al. (2010) that is more suitable for a direct comparison with wake measurements. They adopted Taylor's frozen turbulence hypothesis (Taylor, 1938) and assumed that the large-scale turbulence is correlated across the rotor area. The instantaneous wake position is then given by

$$\frac{\mathrm{d}x_{pre}(t, \Delta T)}{\mathrm{d}t} = \overline{u}_a, \tag{9}$$

$$\frac{\mathrm{d}y_{pre}(t, \Delta T)}{\mathrm{d}t} = v(t, \Delta T), \tag{10}$$

and

$$\frac{\mathrm{d}z_{pre}(t, \Delta T)}{\mathrm{d}t} = w(t, \Delta T), \tag{11}$$

where the subscript "pre" stands for prediction, $\overline{u}_a$ is the downstream advection velocity (also called downstream transport velocity), v and w are the large-scale lateral and vertical turbulent velocity fluctuations, t is the time when a quasi-steady velocity deficit arrives at a downstream location, and ΔT is the time delay until the emitted velocity deficit has reached a given downstream distance. Using the lateral velocity at the turbine location for the right-hand side of Eq. (10), the instantaneous wake center position in the horizontal plane is given by

$$y_{pre}(x, t) = v(t - \Delta T(x))\Delta T(x), \tag{12}$$

where ΔT was expressed as a function of the downstream distance x with

$$\Delta T(x) = \int_0^x \frac{dx}{\overline{u}_a(x)}. \tag{13}$$

We will compare two assumptions for the downstream advection velocity in the results: (1) the advection velocity is the same as mean wind speed with $\overline{u}_a(x) = \overline{u}_{hub}$, and (2) the advection velocity is given by the average of the mean wind speed and mean velocity at the wake center with

$$\overline{u}_a(x) = 0.5(\overline{u}_{cen}(x) + \overline{u}_{hub}) \tag{14}$$

as proposed by Cheng and Porté-Agel (2018). For the latter, the mean velocity at the wake center $\overline{u}_{cen}(x)$ is computed with the analytical wake model of Bastankhah and Porté-Agel (2016) (see Eq. (A2) in appendix A). Assumption (1) is following

the simplified DWMM in Larsen et al. (2008). Assumption (2) is an improvement on Keck (2015), who assumed that the downstream advection velocity is a constant 80% of the mean wind speed.

The vertical component of wake meandering cannot be computed directly, because measurements for the right-hand side of Eq. (11) are not available. Instead, we assume that the vertical wake meandering can be modelled to be proportional to the lateral wake meandering with

$$z_{pre}(x,t) = r_{yz}y_{pre}(x,t),\qquad(15)$$

where the factor r_{yz} is the ratio between the horizontal and the vertical wake meandering strength.

We assume that a suitable choice of r_{yz} is the ratio of lateral to vertical turbulence intensity. For a purely shear driven ABL, ratios of TI_v/TI_u and TI_w/TI_v are about 0.5, while for a purely convective ABL $TI_v \approx TI_u < TI_w$ above the surface layer and $TI_v \approx TI_u > TI_w$ within the surface layer (Moeng and Sullivan, 1994). Wind tunnel experiments with purely shear-driven flows showed that wake meandering in the vertical direction had a smaller amplitude than the lateral direction (España et al., 2012; Bastankhah and Porté-Agel, 2017), which supports the assumed proportionality to the turbulence intensity ratios. Keck et al. (2014a) presented ratios for vertical to lateral wake meandering of approximately 0.6, 0.8, and 0.9 for stable, neutral, and unstable conditions, respectively. We do not have direct measurements of TI_w/TI_v and the data available to us from a nearby meteorological tower was not suitable to determine the boundary layer state. Therefore, we assume $r_{yz} = 0.8$ as an average ratio.

Further, Eq. (15) implies a perfect correlation between y_{pre} and z_{pre}, which might not be the case in reality. However, randomly rearranging z_{pre} changed the slopes of the linear regressions shown in Sect. 3.2 by less than 0.02 (no detectable change for the intercept and the correlation coefficient) and, therefore, does not affect the drawn conclusions.

2.2 Research site and measurement setup

The research site and the measurement setup is the same as reported in Brugger et al. (2022). The setup was implemented between 19 August 2017 and 2 October 2017. Quality assurance and data selection criteria are summarized at the beginning of Sect. 3.

The site consists of an isolated wind turbine located at Kirkwood Community Collage in Cedar Rapids, Iowa (Fig. 2). The wind turbine is a 2.5 MW Liberty C96 from Clipper Windpower with a hub height of $z_{hub} = 79$ m and a rotor diameter of $D = 96$ m. The area in the vicinity of the wind turbine is urbanized with some agricultural farmland to the south and east. Data from the supervisory control and data acquisition (SCADA) system of the wind turbine are available to us with a 10-minute resolution.

We installed two pulsed Doppler LiDARs on the roof of the nacelle (Fig. 3a). A Doppler LiDAR emits infrared laser pulses that are scattered by aerosols within the atmosphere. The backscattered light receives a frequency shift due to the Doppler effect caused by the movement of the aerosols. Assuming that aerosols are transported by the wind, the line-of-sight velocity of the air along the laser beam can be estimated from the frequency shift detected by the instrument. The instruments were Stream Line models from Halo Photonics Ltd. (Worecestershire, UK).

Figure 2. Satellite image of the measurement site with the location of the wind turbine (© Google Earth). The wind turbine coordinates are $41.9165°$ latitude and $−91.6508°$ longitude.

The Doppler LiDAR mounted towards the rear of the nacelle was used to scan the wake. It was configured to average 3000 pulses per velocity estimate and use six points per range gate. This leads to an effective sampling frequency of approximately 3 Hz and spatial resolution of 18 m along the laser beam. A signal-to-noise ratio (SNR) threshold of $−14$ dB is used to reject low quality Doppler LiDAR measurements, resulting in a theoretical standard deviation of the Doppler estimate of 0.3 m s^{-1} as the upper limit for the uncertainty (Pearson et al., 2009). It was programmed to perform 230 successive Plan Position Indicator (PPI) scans in the downstream direction with an opening angle of $\pm12°$ and an azimuth step of $2°$ to capture the wake (Fig. 3). Each individual PPI sweep with the return to the starting position took 7.2 s and the full scan was completed in approximately 28.4 minutes. The scans were designed to be slightly shorter than the 30 minute period allocated in the scan schedule to ensure smooth operation of the measurements. Because the scanner head was moving during the sampling, we assume that the spatial uncertainty of a measurement is equal to its travel distance ($2°$).
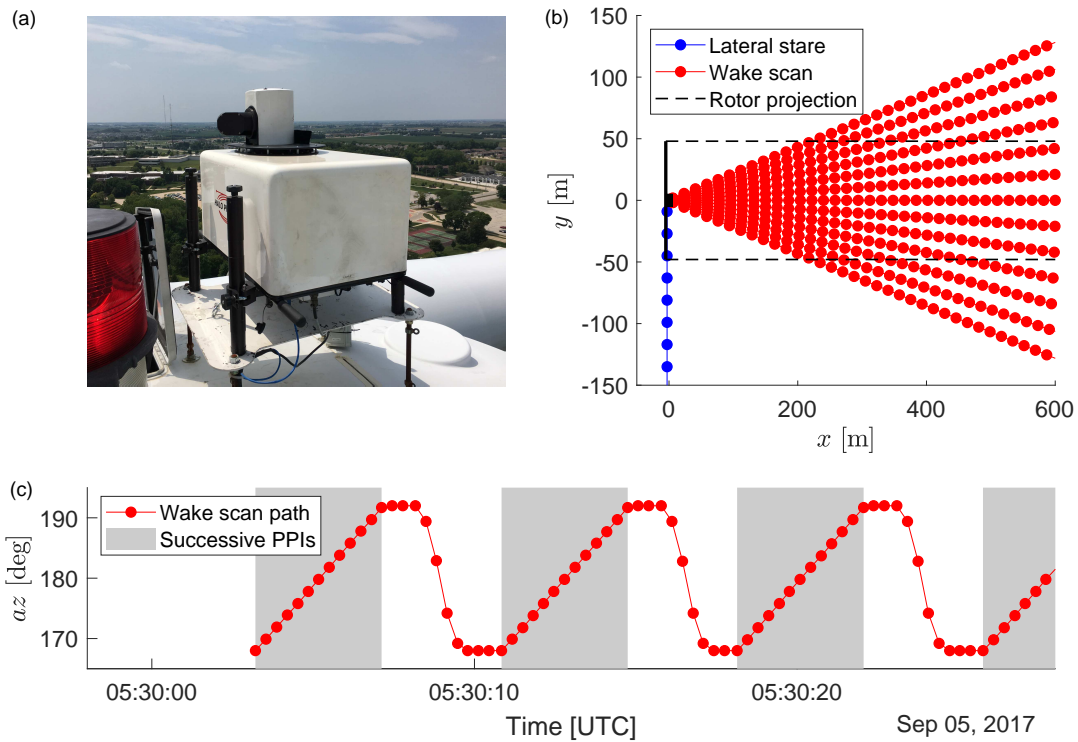
Figure 3. Photo of the front-mounted Doppler LiDAR on the nacelle of the wind turbine (a). Scan patterns of the nacelle mounted Doppler LiDARs viewed from top (b). Wake scans of the rear-mounted Doppler LiDAR (red) were accompanied by measurements in a lateral staring mode of the front-mounted Doppler LiDAR (blue). LiDAR beams are shown as lines with range gate centers indicated as points. The wind turbine is stylized in black and the rotor-edge projection in the wind direction is indicated with black dashed lines. The bottom panel shows the scanner path for a section of a wake scan (c), where the grey area indicates the successive PPIs that, together, become a wake scan. Figure adapted from Brugger et al. (2022) with changes under the Creative Commons Attribution 4.0 License (https://creativecommons.org/licenses/by/4.0/).

Simultaneously, the front mounted Doppler LiDAR was used to measure the inflow. It was configured to average 5000 pulses per velocity estimate and and use six points per range gate. It was programmed to measure the lateral velocity component with a horizontal, fixed beam at a $90°$ to the rotor axis for a period of 14 minutes (for the remainder of the 30 minute period, it measured with a fixed beam parallel to the rotor axis upstream, but those measurements were only used to validate the SCADA data). This scan pattern of the two Doppler LiDARs was scheduled to begin every second hour at the half hour mark. The theoretical uncertainty of the radial velocity was estimated based on the recorded SNR using Eq. (2) from Pearson et al. (2009), but it was smaller than the velocity resolution of the instrument due to the proximity of the range gate from which the data is used (see Sect. 2.3.1). Therefore, the velocity resolution will be assumed as the uncertainty of the lateral velocity (0.038 m s^{-1}).

2.3 Model inputs and reference data

The input values of the DWMM and the reference of the validation use data from separate measurement instruments to keep them independent. The model input is generated from the SCADA data and the measurements of the front-mounted Doppler LiDAR. The measurements of the rear-mounted Doppler LiDAR are used as the reference for the validation.

2.3.1 Model inputs

The input variables of the DWMM and the measurements from which they are taken are listed below:

– $\overline{u}_{hub}$ is the mean wind speed at hub height. It is measured by a cup anemometer located on the roof of the wind turbine and reported in the SCADA data. Because the SCADA data has a 10-minute resolution, we use the average of a 20-minute period for the mean wind speed, which is longer than the 14-minute measurement period of the front-mounted Doppler LiDAR. Based on a comparison to the upstream stare of the front-mounted Doppler lidar, we assume that $\overline{u}_{hub}$ has an uncertainty of 0.25 m s^{-1} quantified as the root-mean-square error.

– $v(t)$ is the time series of the large-scale lateral velocity of the inflow. It is generated from the measurements of the front-mounted Doppler LiDAR using the range gate at a distance of 117 m, which is the closest range gate that is not affected by the rotor. A mean is removed and a low-pass filter with a threshold of $\beta\Delta T$ with $\beta = 0.8$ is applied to isolate the large-scale turbulence fluctuations (Cheng and Porté-Agel, 2018). In the spatial domain, this threshold of the low-pass filter is proportional to the downstream distance x and it is considerably larger than the rotor diameter, which makes it reasonable to assumed that $v(t)$ is representative for the full rotor area. Further, the lateral turbulence intensity (TI_v) and the integral time scale ($T_{i,v}$) are computed from $v(t)$ prior to the low-pass filtering. A proportionality between longitudinal and lateral turbulence intensity with $TI_u = \frac{3}{2}TI_v$ is assumed.

– C_T is the wind speed dependent thrust coefficient of the wind turbine. It is selected from the thrust curve in Fig. A1 based on $\overline{u}_{hub}$.

2.3.2 Reference data set

The instantaneous wake center position, the turbulence intensity added by wake meandering, and the reduction of the mean velocity deficit due to wake meandering are extracted from the measurements of the rear mounted Doppler LiDAR. The processing steps listed below and illustrated in Fig. 4 are similar to those in Brugger et al. (2022):

1. The line-of-sight velocities are gridded on a polar coordinate system $u_r(\phi, r, t)$ with an azimuth (ϕ) resolution of $2°$, a radial (r) resolution of 18 m, and a time step (t) aligning with the PPIs of the wake scans. The az positions of the LiDAR scans and the ϕ positions of the polar coordinate system can have a difference of $0.2°$ towards the end of a PPI resulting from the acceleration phase of the scanner head, small variations of the scanner behaviour, and fluctuations of the sampling frequency. Multiple measurements are available for the outside grid points due to a short resting time of the scanner at the turn-around point and the measurements closest in time are used at those grid points.
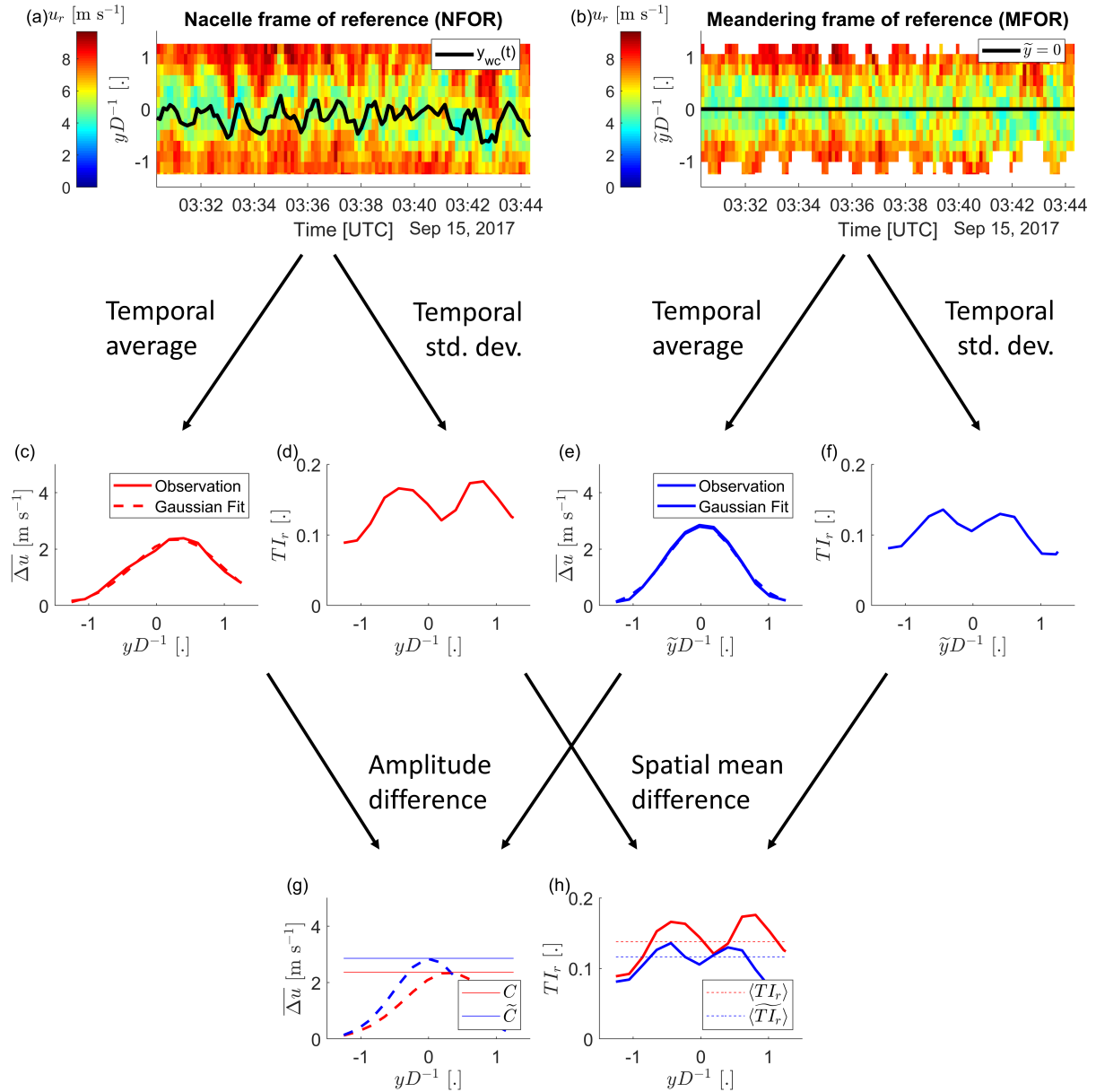
Figure 4. The data processing steps to quantify the effect of wake meandering on the mean velocity deficit and the turbulence intensity are illustrated for an example at a downstream distance of $x = 5D$. The instantaneous velocity deficit in the nacelle frame of reference (a) and meandering frame of reference (b) have a temporal average (c, e) and standard deviation (d, f) applied. The reduction of the mean velocity deficit due to wake meandering is then quantified as amplitude difference (g) of two Gaussian fits to the two velocity deficits in (c) and (e). The turbulence intensity added by wake meandering is quantified as the spatially averaged difference in turbulence intensity (h).

2. The transformation to a Cartesian coordinate system is made using $y = r\sin^{-1}(\phi)$ and $x = \langle r\cos^{-1}(\phi)\rangle$, where the angle brackets indicate the lateral averaging.

3. An instantaneous velocity deficit is computed with $\Delta u_r(x,y,t) = \overline{u}_{hub} - u_r(x,y,t)$. This approach maps all measurements during a PPI on a single time stamp neglecting the travel time of the scanner head.

4. The instantaneous position of the wake center is detected with the centroid of the velocity deficit with

$$y_{wc}(x,t) = \frac{\sum_y y\Delta u_r(x,y,t)}{\sum_y \Delta u_r(x,y,t)}, \tag{16}$$

where the subscript "wc" stands for wake centroid and negative values of $\Delta u_r(x,y,t)$ are set to zero.

5. The instantaneous velocity deficit in the meandering frame of reference ($\Delta u_r(x,\tilde{y},t)$) is computed by transformation of the lateral coordinate with $\tilde{y} = y - y_{wc}$ and interpolated on the original y grid points.

6. The temporal mean and the standard deviation of $\Delta u_r(x,y,t)$ and $\Delta u_r(x,\tilde{y},t)$ provide profiles of the mean velocity deficit and the turbulence intensity in the nacelle frame of reference (NFOR) and the meandering frame of reference (MFOR), respectively. The NFOR is identical to a fixed frame of reference here, because data was selected to have no yaw activity of the wind turbine.

7. The reduction of the mean velocity deficit due to wake meandering is then quantified by the amplitude difference of two Gaussian functions fitted to the mean velocity deficit in the NFOR and the MFOR, respectively. The difference will be denoted as $\widetilde{C} - C$ where C ($\widetilde{C}$) is the amplitude of the Gaussian function in the NFOR (MFOR).

8. The turbulence added by wake meandering is quantified by the laterally averaged difference in turbulence intensity between the NROR and the MFOR. It will be denoted as $\langle TI_u - \widetilde{TI}_u\rangle$.

9. Lastly, a temporal mean is also removed $y_{wc}(x,t)$ and a low-pass filter is applied to make it comparable to $y_{pre}(x,t)$ of the DWMM that is based on the detrended and low-pass filtered $v(t)$.

The above processing steps are applied for downstream distances between $xD^{-1} = 3$ and $xD^{-1} = 7$. The Doppler lidar's field of view and the double-peak shape of velocity deficit in the near-wake were problems for the detection of y_{wc} for $xD^{-1} < 3$, and the lateral resolution of the lidar scans became coarser than 10 m for $xD^{-1} > 7$. Some parts of the results will focus on a downstream distance of $x = 5D$, because the scanning cone has an ideal width of $2D$ there and $5D$ is typical distance between wind turbines in onshore wind farms.

2.3.3 Error propagation of the measurement uncertainty

The measurement uncertainties are propagated to the model predictions and the reference data with a Monte Carlo method. We created 100 resamples of the measurement data with random fluctuations added that were drawn from a normal distribution with a standard deviation equal to the measurement uncertainty (except for the azimuth for which a uniform distribution was used).

The model predictions and the wake quantities were computed for each of the 100 resamples and the propagated measurement uncertainty was quantified as the root-mean-square error. If results are normalized in Sect. 3, we apply the error propagation rules for a division as a last step.

In case of the DWMM, the Monte Carlo approach was implemented in two stages. First, we estimated the uncertainty of y_{pre} with the Monte Carlo approach based on the uncertainties of v and $\overline{u}_{hub}$. Then, we estimated the uncertainty of the mean velocity deficit and the added turbulence intensity with a second Monte Carlo approach based on the uncertainties of y_{pre} and $\overline{u}_{hub}$.

3 Results

The first part of the results will focus on the modelling of wake meandering itself, while the second part will focus on the validation of the predicted effects that wake meandering has on the mean velocity deficit and the turbulence intensity. A set of 43 cases, each covering an approximately 14-minute period, was selected from the measurement data of the campaign. The selection criteria were a mean wind speed above 5 m s^{-1}, no yaw movement of the wind turbine, a sufficient mean SNR of the Doppler lidar, and a wake within the Doppler lidar's scanning cone. The 43 cases cover a wind speed range from 5 m s^{-1} to 11 m s^{-1}, turbulence intensities of the lateral velocity component up to 8% (for higher turbulence intensities, the wake is not covered by the Doppler LiDARs scanning cone due to very strong wake meandering). The selection criteria and the data set are identical to Brugger et al. (2022).

3.1 Testing of the passive scalar assumption of the DWMM

First, the predictions of the instantaneous wake center positions will be validated. The root-mean-square error (RMSE) and the correlation coefficient between the predicted wake center position (Eq. 12) and the observed wake center position (Eq. 16) will be used as quality metrics. The observed wake center position has been low-pass filtered with the same filter threshold as the input of the DWMM for comparability. The results of the evaluation at $x = 5D$ are shown in Fig. 5. They have a general trend of an increasing correlation and a decreasing normalized RMSE with $T_{i,v}\Delta T^{-1}$. The ratio $T_{i,v}\Delta T^{-1}$ quantifies the rate of evolution of the turbulent wind field during the time of downstream advection (or in other words how well the Taylor's frozen turbulence hypothesis holds). This behaviour is in agreement with the recommendation that for large downstream distances, the spatial variability of the large-scale turbulence components should be taken into account (Larsen et al., 2008), which is supported by the results of a previous data analysis (Brugger et al., 2022).

Next, we will investigate the effect of the downstream advection velocity on the predicted wake-center positions. We will compare predictions using the reduced downstream advection velocity given by Eq. (14) with predictions using the mean wind speed of the inflow as the downstream advection velocity. The effect of the choice of advection velocities on the correlation coefficient is shown in Fig. 6a. It shows that using $\overline{u}_a$ instead of $\overline{u}_{hub}$ improved the correlation between predictions and observations for $x < 5D$, indicating better temporal alignment for the predictions using the reduced downstream advection velocity. Removing a temporal trend instead of the mean from y_{pre} and y_{wc} prior to the correlation would lead to a twice as
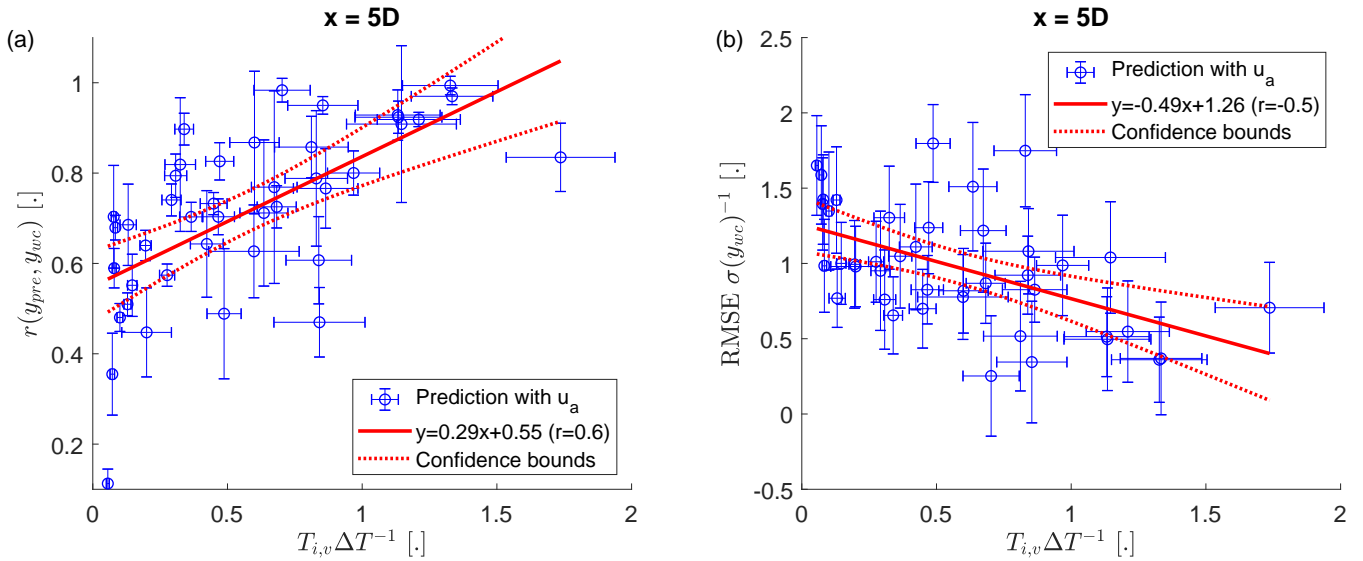
Figure 5. The correlation coefficient (a) and normalized root-mean-square error (b) between the wake center position predicted by the dynamic wake meandering model (y_{pre}, Eq. 12) and the observed wake position by the wake scanning Doppler lidar (y_{wc}, Eq. 16) at a downstream distance of $5D$ from the wind turbine. The ratio between the integral time scale of lateral velocity ($T_{i,v}$) and the time delay due to downstream advection (ΔT^{-1}) quantifies the rate of evolution of the turbulent wind field during the time of downstream advection. The error bars show the standard deviation of the propagated measurement uncertainty. The 95% confidence bounds of the linear fit show the statistical uncertainty due to the scatter of the data points.

large improvement of the correlation (we do not remove a linear trend here, because it is problematic for Sect. 3.2 where we cannot remove a trend from the observations). This can be explained by non-steady effects like a change of the wind direction, which contribute to the correlation, but do not depend on the downstream transport. No systematic effect on the correlation is observed beyond $5D$, which can be explained by $\overline{u}_a(x)$ approaching $\overline{u}_{hub}$ with increasing x and the decorrelation of the two turbulent signals with increasing separation.

Despite the increase in correlation coefficient, using $\overline{u}_a$ had a detrimental effect on the normalized RMSE (Fig. 6b). This will be investigated in more detail in the following section.

3.1.1 Overestimation of the wake meandering strength

It was previously observed that using $\overline{u}_a$ as the advection velocity increases the RSME despite having a higher correlation with the observation. Analysing several cases visually, we observed that the predictions had in many cases a too large amplitude of the wake displacement compared to the observations. Figure 7 shows three examples from the data set to illustrate the behaviour. It is apparent that the better temporal alignment of the predictions using $\overline{u}_a$ is accompanied by an overestimation of the wake displacement compared to the predictions with $\overline{u}_{hub}$. Quantifying the overestimation with the difference in wake
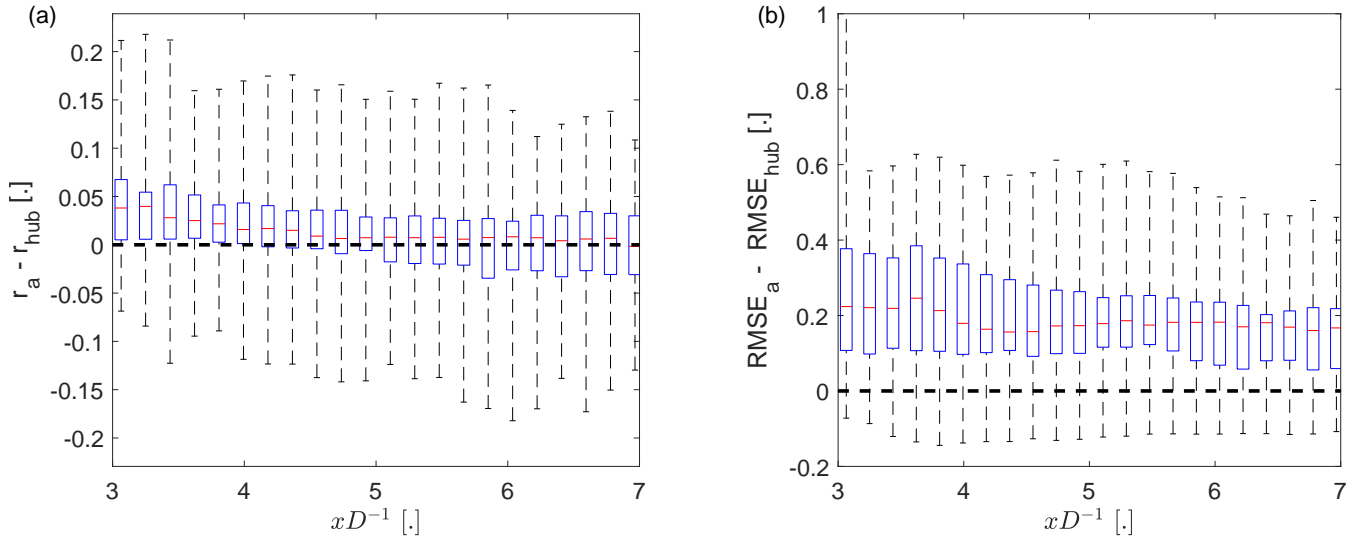
Figure 6. The effect of the downstream advection velocity on the correlation coefficient (a) and on the normalized root-mean-square error (b) between y_{pre} and y_{wc} as a function of the downstream distance. The subscript "a" ("hub") indicates $\overline{u}_a$ ($\overline{u}_{hub}$) as downstream advection velocity. The whiskers show the range of the data, the top and bottom of the blue box indicating the 25th and 75th percentile, and the red center marker showing the median.
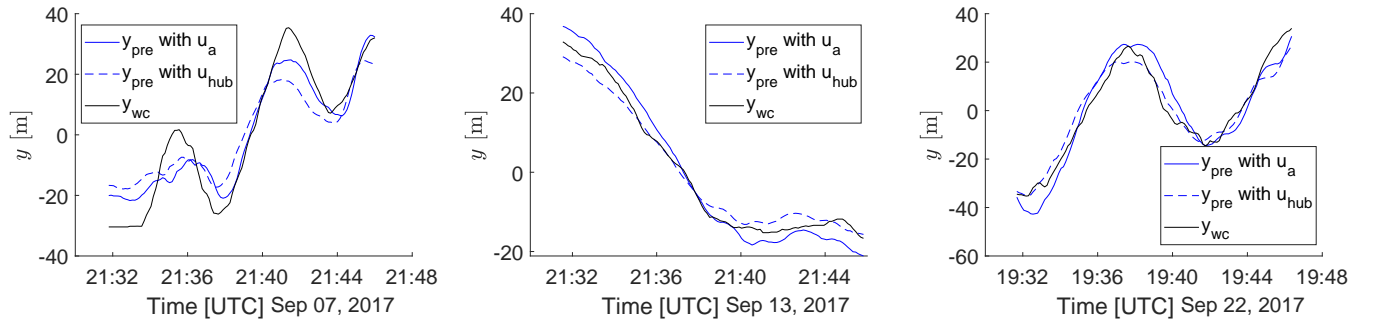
Figure 7. The time series of the observed and the predicted wake center positions at $x = 5D$ for three example cases, which were selected for their high correlation between reference and prediction. The predictions are shown for $\overline{u}_{hub}$ (dashed blue) and $\overline{u}_a$ (solid blue) as the downstream transport velocity. The reference from the observations is shown in black.

meandering strength for the whole data set, it becomes clear that this is a systematic bias that is introduced by the reduced advection velocity (compare Fig. 8a and Fig. 8b).

Better temporal agreement of the DWMM when using a downstream advection velocity slower than the mean wind speed was observed in several studies (Bingöl et al., 2010; Keck et al., 2014b; Machefaux et al., 2015). However, a subsequent
290 overestimation of the wake meandering strength has not been reported as a problem so far. While Keck et al. (2014a) showed in their Fig. 3 that the lateral wake meandering strength predicted by the DWMM increases with a slower downstream transport
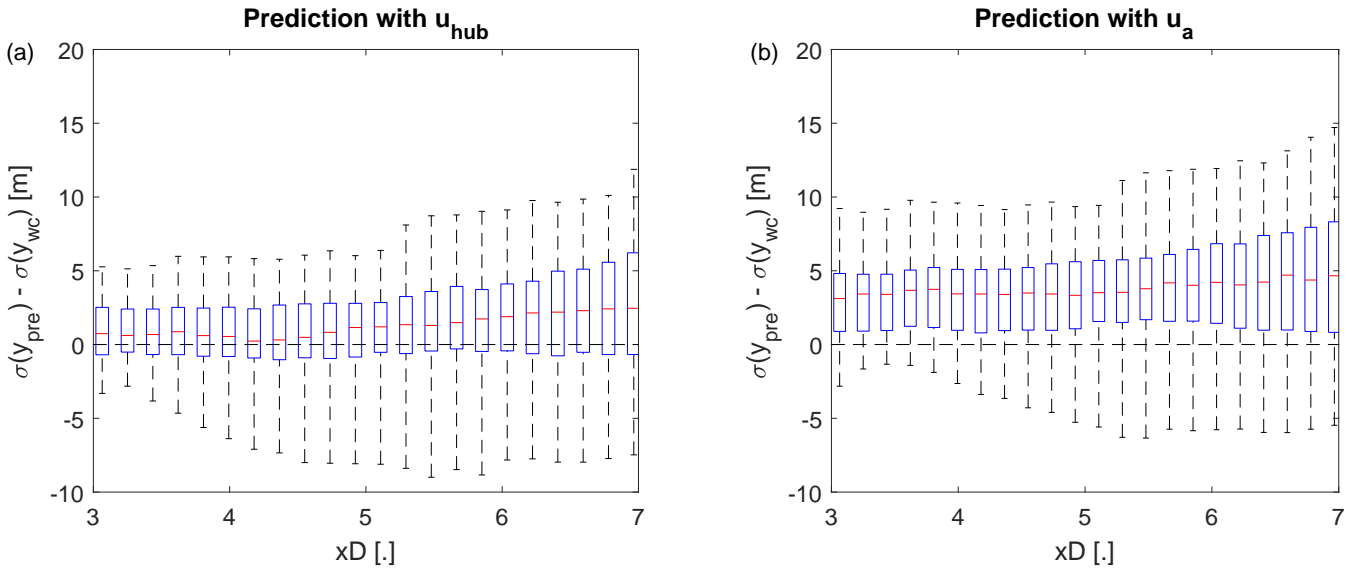
Figure 8. Error between observed and predicted wake meandering strength with $\overline{u}_{hub}$ (a) and $\overline{u}_a$ (b) as downstream advection velocity. The whiskers show the range of the data, the top and bottom of the blue box indicate the 25th and 75th percentile, and the red center marker shows the median.

velocity for $x < 10D$, they did not further investigate the matter (possibly due to a scaling of the wake meandering strength at a later stage of their DWMM implementation). In a previous validation of the passive scalar assumption by Bingöl et al. (2010), this phenomenon was not reported, but a visual inspection of their Fig. 8 suggests that three of their four cases also exhibit a larger displacement of the wake center position in the DWMM predictions compared to the wake measurements. Trujillo et al. (2011) showed an example case in their Fig. 5 which we digitized (linearly interpolating the parts that where obstructed by other plot elements) and found similar displacements of the wake center position for the predictions and the observations. However, the description of their data processing mentions low-pass filtering only for the modelled wake of the DWMM and not the observed wake, which could mask the overestimation. Other validations might not have observed this issue previously, because using the mean wind speed for the downstream advection and a temporally averaged validation approach masks the issue (Reinwardt et al., 2018, 2020; Conti et al., 2021).

Based on our own findings and the literature review, we believe that the discrepancy between temporal agreement and wake meandering strength points towards a short-coming of the passive-tracer assumption of the DWMM. In the following section, we will provide a hypothesis to addresses this problem. Other possible explanations for the overestimation that were tested on the data and rejected are listed in appendix B.

3.1.2 Improvement of the DWMM to account for momentum transport

We hypothesize that the transport of the wake with large-scale turbulence is more akin to the transport of momentum than the transport of a passive tracer and that, subsequently, the turbulent Schmidt number should be considered in the modelling of wake meandering. The turbulent Schmidt number characterises the ratio between the turbulent transport of momentum and the turbulent transport of passive scalars. Previous experiments indicated that momentum is transported less efficiently than scalars in turbulent wakes (Reynolds, 1976; Antonia et al., 1993). First, we provide support for this hypothesis by comparing observed transport behaviour of the wake with the expectation of a passive scalar. Then we include the turbulent Schmidt number into the DWMM and compare those new predictions with the observations.

We use the diffusion theory of Taylor (1922) to compare the observed transport of wake meandering with the expected transport of a scalar. Cheng and Porté-Agel (2018) adapted the diffusion theory from a point source to an area source for wind turbine wakes. The standard deviation of a lateral profile of a scalar concentration in a wake at Δx downstream of the virtual point source is then given by

$$\sigma_{y,scalar} = \left\langle v^2 \right\rangle^{0.5} \frac{\Delta x}{\overline{u}_a}, \tag{17}$$

where $\left\langle v^2 \right\rangle^{0.5}$ is the standard deviation of the lateral air velocity. If momentum is considered, which is transported less efficient than a scalar in a wake (Reynolds, 1976), this expression becomes

$$\sigma_{y,wake} = \sqrt{Sc_t} \left\langle v^2 \right\rangle^{0.5} \frac{\Delta x}{\overline{u}_a}, \tag{18}$$

where Sc_t is the turbulent Schmidt number. We assume that the standard deviation of the lateral transport velocity of the wake centroid can be expressed as $\left\langle v_{wake}^2 \right\rangle^{0.5} = \sqrt{Sc_t} \left\langle v^2 \right\rangle^{0.5}$. With this assumption, we can determine the turbulent Schmidt number of wake meandering from the ratio of the standard deviation of the lateral velocity to the standard deviation of the lateral velocity of the wake centroid:

$$Sc_t = \left(\left\langle v_{wake}^2 \right\rangle^{0.5} \left\langle v^2 \right\rangle^{-0.5} \right)^2. \tag{19}$$

The lateral transport velocity of the wake center (v_{wake}) can be determined from the lateral displacement of the wake center position following a method of Machefaux et al. (2015). First, the time lag Δt between $v(t)$ and the wake center position $y_{wc}(t)$ for a given downstream distance is determined with a cross-correlation. We do not use Eq. (13) to compute the time delay to make no assumptions on the downstream transport velocity here. Then, the lateral transport velocity of the wake center is estimated with $v_{wake} = y_{wc}/\Delta t$. If the cross-correlation for determining Δt is lower than 0.8 the estimate of v_{wake} is rejected.

The turbulent Schmidt number was determined with Eq. (19) using v measured by the front-mounted Doppler lidar as described in Sect. 2.3.1 and v_{wake} determined as described in the previous paragraph. Both time series were low-pass filtered and detrended to make them comparable. The results in Fig. 9 show that the turbulent Schmidt numbers of wake meandering are smaller than unity for the majority of the data set. The average of the observed Sc_t is 0.71, which is close to 0.7 used by Cheng and Porté-Agel (2018) for wind turbine wakes based on Reynolds (1976). This suggests that wake meandering is
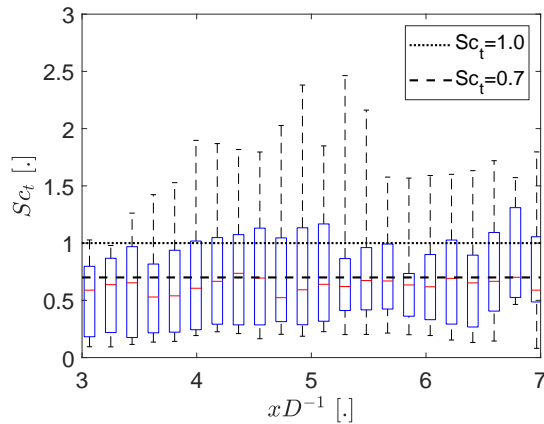
Figure 9. Turbulent Schmidt numbers of wake meandering (Eq. 19) as function of the downstream distance from the wind turbine. The whiskers show the range of the data, the top and bottom of the blue box indicate the 25th and 75th percentile, and the red center marker shows the median.

more akin to the transport of momentum than the transport of a passive scalar. Using an average over multiple range gates to determine v to mirror the spatial averaging of the wake center detection changes the average Sc_t to 0.69. Down sampling v to the temporal resolution of y_{wc} prior to low-pass filtering has also only a small effect on the results by changing the average Sc_t to 0.64.

Following our hypothesis, we modified the DWMM to account for a reduced momentum transport efficiency by including $\sqrt{Sc_t}$ with constant $Sc_t = 0.7$ in Eq. (12). The results are shown in Fig. 10. Including Sc_t reconciled 89% of the overestimation of the wake meandering strength.

3.2 Validation of the modified DWMM

The second part of the results will validate the predictions of the DWMM for the effect of wake meandering on the mean velocity deficit and the added turbulence intensity. The DWMM will be compared to the observations in Sect. 3.1.2 and the impact of the previously proposed modification will be investigated in Sect. 3.2.2. The validation is focused on the effect of wake meandering instead of the absolute values, because the absolute values can be predicted with an analytical model (e.g Qian and Ishihara, 2018) and the ability to predict the effect of wake meandering sets the DWMM apart.

3.2.1 Prediction of the mean velocity deficit and the turbulence intensity

First, we validate the predicted reduction of the mean velocity deficit due to wake meandering. The modified DWMM treating the wake as non-passive (i.e. using $\overline{u}_a$ as the downstream advection velocity and $Sc_t = 0.7$) is shown in Fig. 11a and compared to the observations in Fig. 11b. While both show that the recovery of the mean velocity deficit increases with the wake meandering strength, there is a main difference between the model and the observations: for a weak wake meandering strength (small values of $\sigma(y_{wc})D^{-1}$) the observations scatter around zero, but the model has strictly positive values. This causes the
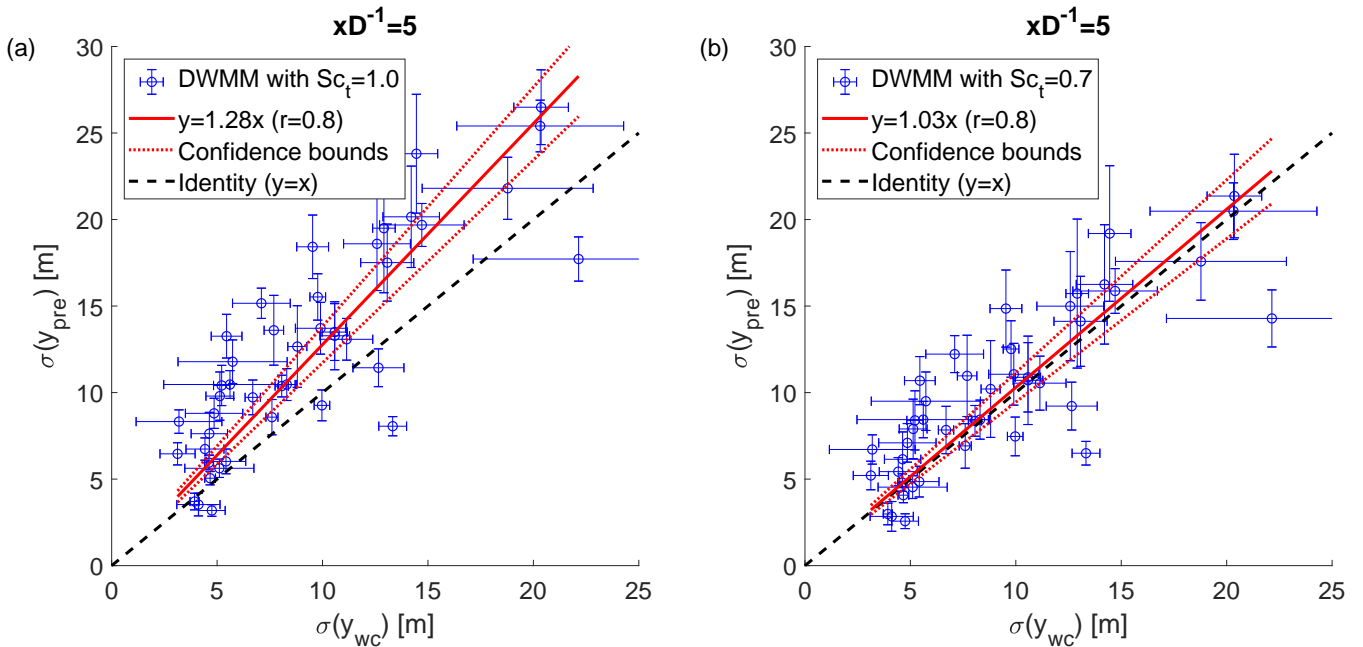
Figure 10. Observed wake meandering strength and predicted wake meandering strength of the DWMM. The left panel (a) shows the DWMM with the passive scalar assumption and the right panel (b) shows the DWMM modified with turbulent Schmidt number to account for a less efficient momentum transport. The errorbars show the standard deviation of the measurement uncertainty propagated to the predicted and observed wake meandering strength, respectively. The 95% confidence bounds of the linear fit show the statistical uncertainty due to the scatter of the predictions.

model to have a smaller slope in a linear regression and a larger intercept compared to the observations. The negative values in the observations can be explained by the method of isolating the effect of wake meandering. Random fluctuations of the detected wake center position due to measurement errors, measurement resolution, and morphing of the wake introduce more variability into the MFOR than just the small-scale turbulence alone. If the wake meandering is weak, this erroneous variability

360   in the MFOR can be of the same magnitude as the variability in the NFOR, thus leading to values scattering around zero.

Next, the model predictions of the added turbulence intensity due to wake meandering are validated. We observe that both the modified DWMM and the observations show an increase of the added turbulence intensity with the wake meandering strength (Fig. 12a and Fig. 12b). Similar to the mean velocity deficit in the previous paragraph, the predictions of the DWMM are strictly positive for weak wake meandering, while the observations scatter around zero. This leads to a smaller slope and

365   larger intercept for the model compared to the observations. The reason is that for weak wake meandering, the difference in turbulence intensity between the MFOR and the NFOR becomes very small and the aforementioned variance in the MFOR from other sources than small-scale turbulence affecting the observations lead to a scattering around zero.
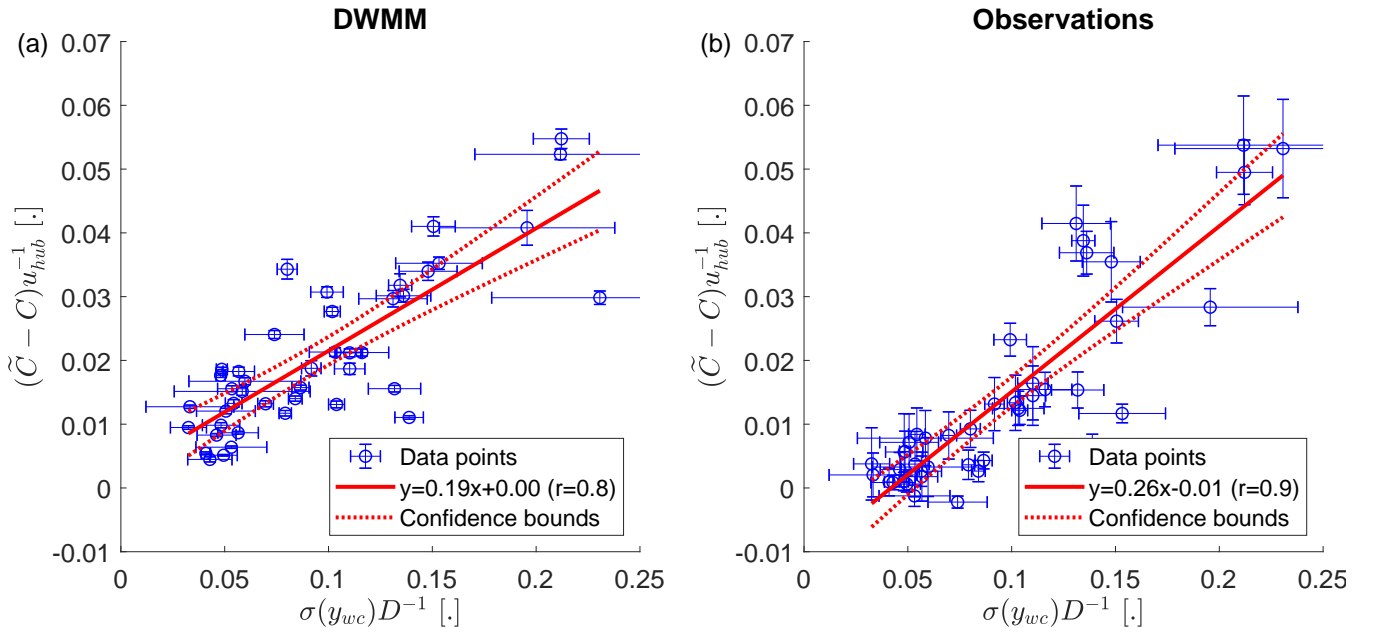
Figure 11. The reduction of the mean velocity deficit as a function of the wake meandering strength at a downstream distance of $x = 5D$. Panel (a) shows predictions of the modified DWMM using $\overline{u}_a$ as the downstream advection velocity with a turbulent Schmidt number of $Sc_t = 0.7$ and panel (b) shows the observations. The error bars show the standard deviation of the measurement uncertainty propagated to the observed wake meandering strength or the predicted velocity deficit reduction, respectively. The 95% confidence bounds of the linear fit show the statistical uncertainty due to the scatter of the data points.

3.2.2 Effect of modifications to the DWMM

To investigate the effect of the proposed modification to the DWMM on the comparison with the observations, we compare three versions of the DWMM:

1. The original DWMM using the passive tracer assumption ($\overline{u}_{hub}$ as the downstream advection velocity and $Sc_t = 1.0$).

2. A semi-modified DWMM that only accounts for the slower downstream advection velocity without modifying the lateral transport ($\overline{u}_a$ as the downstream advection velocity and $Sc_t = 1.0$). This is in line with recommendations in the literature for the application of the DWMM that suggest a downstream transport velocity slower than the mean wind speed, but do not mention further changes to the lateral and vertical transport equations of the DWMM (Bingöl et al., 2010; Brugger et al., 2022).

3. The fully-modified DWMM as proposed here that treats the wake as non-passive ($\overline{u}_a$ as the downstream advection velocity and $Sc_t = 0.7$).

Table 1 shows the root-mean-square error of a direct comparison between the observations and the three versions of the DWMM. We observe from Table 1 that (i) the original DWMM and the fully-modified DWMM have similar errors to the
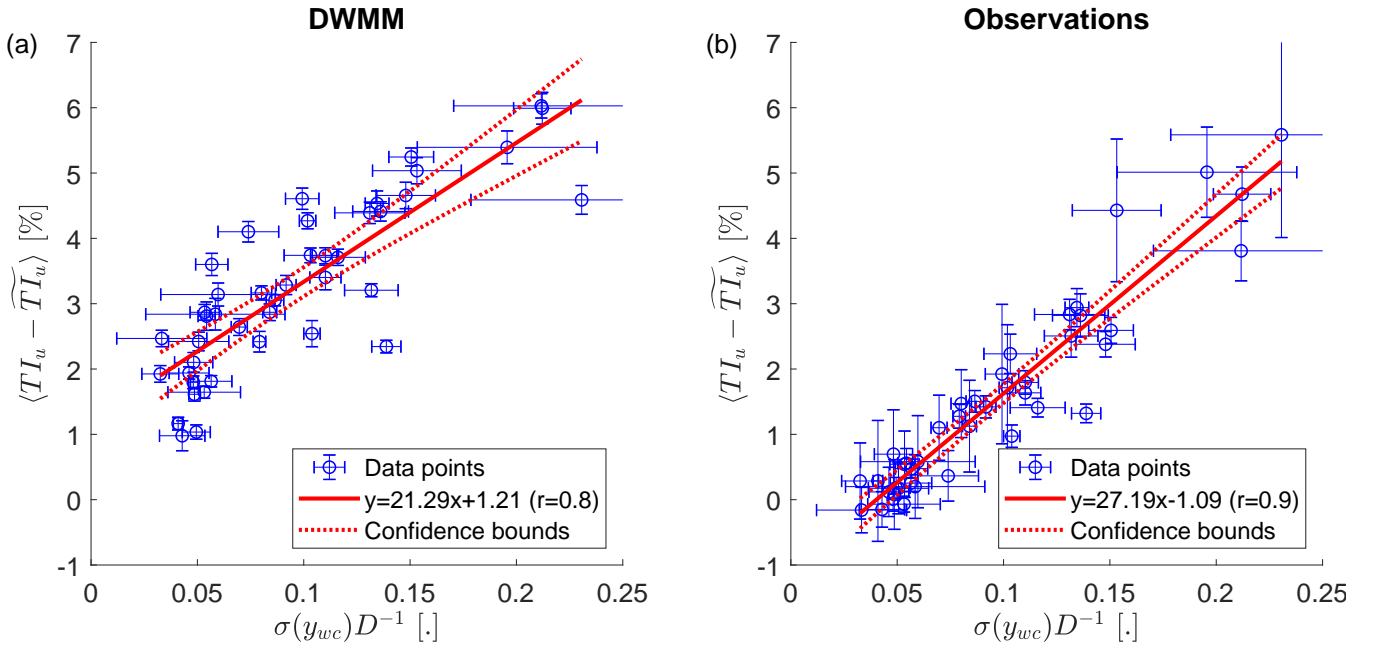
Figure 12. The added turbulence intensity as a function of the wake meandering strength at a downstream distance of $x = 5D$. Panel (a) shows predictions of the modified DWMM using $\overline{u}_a$ as the downstream advection velocity with a turbulent Schmidt number of $Sc_t = 0.7$ and panel (b) shows the observations. The error bars show the standard deviation of the measurement uncertainty propagated to the observed wake meandering strength or the predictions of the added turbulence intensity, respectively. The 95% confidence bounds of the linear fit show the statistical uncertainty due to the scatter of the data points.

observations, and that (ii) the semi-modified DWMM has a considerably larger error. This is the case for the effect of wake meandering on the mean velocity deficit as well as for the added turbulence intensity.

The similar results for the original DWMM and the fully-modified DWMM are explained by the temporally averaged validation approach used here, where the errors of a too fast downstream transport and a too efficient lateral transport mostly cancel out, which might also explain why the issue was not noticed in previous validations. Only when including dynamics into the validation as in Sect. 3.1, the benefit of non-passive implementation of the DWMM becomes apparent.

The considerably larger error of the semi-modified DWMM compared to the other two implementations is explained by the overestimation of the wake meandering strength observed in Sect. 3.1.1 that leads to an overestimation of its effect on the mean velocity deficit and the turbulence intensity. This indicates that only using a slower downstream transport velocity in the DWMM is not fully accounting for the non-passive nature of the wind turbine wake. Lastly, it should be mentioned that the semi-modified DWMM is also treating the wake inconsistently by using $\overline{u}_a$ (non-passive in the x direction) and $Sc_t = 1.0$ (passive in the y and z direction). Including the Schmidt number is required to accurately represent momentum transport in the wake.

Table 1. The root-mean-square error (RMSE) between the observations and three versions of the DWMM. The left column shows the error percentage for the reduction of the normalized mean velocity deficit due to wake meandering ($\widetilde{C} - C$), and right column shows the error of the turbulence intensity added by wake meandering ($\langle TI_u - \widetilde{TI}_u \rangle$). All values were computed at a downstream distance of $x = 5D$.

	$\widetilde{C} - C$	$\left\langle TI_u - \widetilde{TI}_u \right\rangle$
Original DWMM (u_{hub}, $Sc_t = 1.0$)	2.42	1.91
Semi-modified DWMM (u_a, $Sc_t = 1.0$)	3.29	2.58
Fully-modified DWMM (u_a, $Sc_t = 0.7$)	2.38	1.89

4 Conclusions

395   A test of the existing formulation of the DWMM and a new formulation that incorporated additional physics was presented. The test site was an isolated wind turbine in Cedar Rapids, Iowa. A Doppler lidar deployed on the nacelle of the wind turbine scanning the velocity field of the wake at hub height was used as reference to which the models were compared. A second Doppler lidar and the SCADA data of the wind turbine was used to initialize the wake meandering models.

The results for the instantaneous wake center position exposed an issue with the passive tracer assumption of the existing
400   formulation of the DWMM. The wake meandering strength had better agreement with the observation, if the mean wind speed is used for the downstream transport, while at the same time, a better temporal agreement is reached if the downstream transport used a special wake velocity to more accurately represent the advective transport. Analysing the transport behaviour of the wake, we found that both the downstream transport of wake meandering as well as the lateral wake displacement showed differences compared with the DWMM assuming a passive scalar transport. Therefore, we propose to include the turbulent
405   Schmidt number in the DWMM to account for the less efficient turbulent transport of momentum compared to a passive scalar in addition to the a slower downstream transport velocity. This will also make the DWMM physically more consistent, because the wake is considered fully non-passive with this modification, while previously it has been treated as non-passive in the downstream direction and passive in radial direction.

A comparison of the thus modified DWMM with measurements showed that it reconciles the previously noted discrepancy
410   of statistics and dynamics. The DWMM using only the more accurate downstream transport velocity had an error increase of 35% for the mean velocity deficit reduction and 36% for the added turbulence intensity compared to the original DWMM using the passive tracer assumption. The DWMM that included the Schmidt number in addition to the more accurate downstream transport velocity had an error reduction for those statistics by 2% and 1%, respectively (and better temporal agreement for the dynamics of wake meandering).

415   In future work, we propose a validation of our findings with a different experimental approach or through simulations to exclude site factors or methodological biases. It would also be interesting to investigate if the variability in the MFOR can be fully explained with the small-scale turbulence part of the DWMM. However, the latter requires wake measurements with a higher temporal and spatial resolution.

Data availability. The data is currently prepared to be published on Zenodo.

420 Appendix A: Equations of the Bastankhah and Porté-Agel (2016) model

The normalized mean velocity deficit of the Bastankhah and Porté-Agel (2016) model for a wind turbine aligned with the mean wind direction is given by

$$\frac{\Delta \overline{u}}{\overline{u}_{hub}} = A(x) \exp\left(-\frac{1}{2}\frac{y^2 + z^2}{\sigma^2}\right), \tag{A1}$$

where A is the normalized mean velocity deficit at the wake center and σ is the wake width. The normalized mean velocity
425 deficit at the wake center is given by

$$A(x) = \left(1 - \sqrt{1 - \frac{C_T}{8\sigma(x)^2/D^2}}\right) \tag{A2}$$

with the thrust coefficient C_T. The thrust curve for this turbine model is not available to us and we will use an ensemble averaged thrust curve of several wind turbine models given there general similarity of C_T between different wind turbines (Fig. A1). The C_T is then chosen from the assumed thrust curve based on $\overline{u}_{hub}$. The wake width is given by

$$430 \quad \sigma(x) = k^* \frac{(x - x_0)}{D} + \frac{1}{\sqrt{8}}, \tag{A3}$$

where x_0 is the near wake length and k^* is the wake growth rate. The growth rate is computed with $k^* = 0.35TI_u$ assuming the linear relationship between k^* and the turbulence intensity found by Carbajo Fuertes et al. (2018). The near wake length x_0 is given by

$$x_0 = \frac{1 + \sqrt{1 - C_T}}{\sqrt{2}(\alpha^* TI_u + \beta^*(1 - \sqrt{1 - C_T}))}, \tag{A4}$$

435 where $\alpha^* = 2.32$ and $\beta^* = 0.154$. For the computation of the advection velocity in Eq. (14) we use $\overline{u}_{cen}(x) = \overline{u}_{hub}(1 - A(x))$ with $A(x)$ given by Eq. A2 the assumption that $A(x_0)$ is valid for $x < x_0$.

Appendix B: Tested hypotheses for the overestimation of the wake meandering strength

The following hypotheses for the overestimation of the wake meandering strength observed in Sect. 3.1.1 were tested:

- Temporal variations of the downstream advection velocity during a 14-minute period would lead to a reduced (increased)
440   amplitude of the wake meandering during times with faster (slower) than average advection velocity. Utilizing the outside points of PPI of the wake scanning LiDAR to gain a time series of the wind speed, we found that the effect on the predicted wake center position is too small to explain the overestimation.

- A misalignment of the wind turbine could contaminate the lateral velocity measured by the front-mounted Doppler LiDAR with contributions from the longitudinal velocity. We used the yaw angle reported in the SCADA data, and the
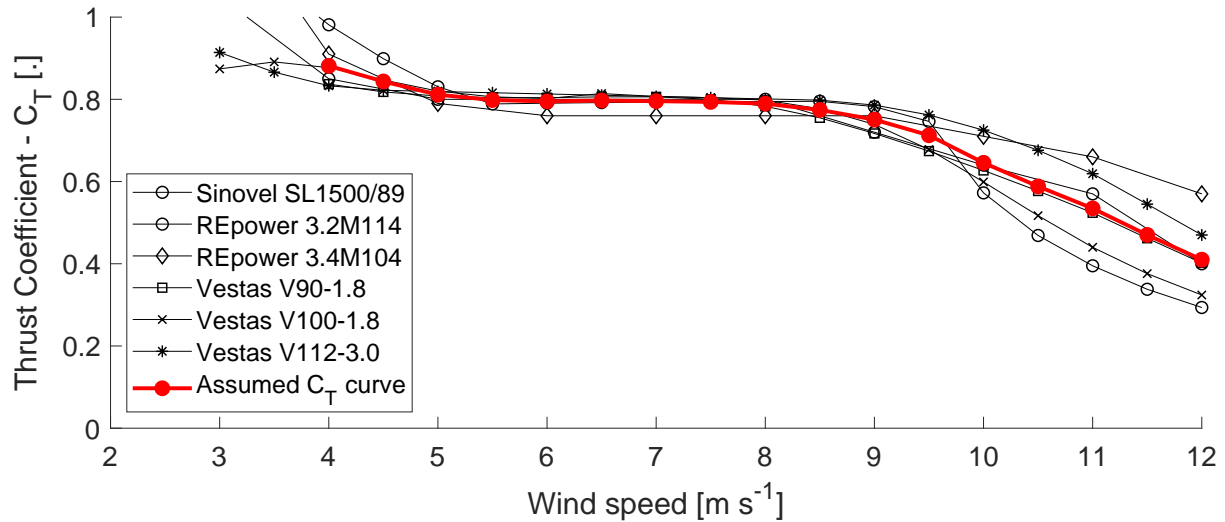
Figure A1. Thrust coefficient curves of six wind turbines from manufacturer data (first compiled by Abdulrahman, 2017) and the ensemble average, which is assumed as the C_T curve for wind turbine at the measurement site. Figure reused from Brugger et al. (2020) without changes under the Creative Commons Attribution 4.0 License (https://creativecommons.org/licenses/by/4.0/).

445   mean wake center position within the wake scanning LiDAR's field of view to quantify the yaw misalignment of the wind turbine. The overestimation did not show any relationship to both neither in average nor trend.

– The overestimation persists if the mean instead of a linear trend is removed from v and y_{wc}. A decrease in magnitude in case of a removed linear trend is explained by removing the largest scales of turbulence.

– In case any remaining flow distortion of the wind turbine affecting $v(t)$ went unnoticed, range gates at a greater distance
450   than $y = 117$ m were tested, but the overestimation persisted.

– We had the hypotheses that the onset of wake meandering is delayed due to a sheltering effect within the near wake until entrainment has reached the wake center. However, this assumption seems unrealistic based on the fact that the wake scanning LiDAR shows wake meandering within the near wake. Testing hypotheses on the data led to a increased of the RMSE for $xD^{-1} < 5$ due to an underestimation of the wake meandering there, and small decrease of the RMSE at
455   greater x.

Author contributions. P.B. contributed to the data curation, formal analysis, conceptualization, methodology, software, validation, visualization, and writing (original draft). F.P.-A. contributed to the conceptualization, funding acquisition, project administration, supervision, and review and editing). C.D.M contributed to the funding acquisition, resources, data curation, investigation, and review and editing.

Competing interests. The authors declare that they have no conflict of interest.

460 *Acknowledgements.* The authors would like to thank Kirkwood Community College for their cooperation and allowing access to their wind turbine. We also extend our appreciation to Clipper Windpower for granting access to technical data on the Liberty wind turbine. This research was funded by the Swiss National Science Foundation (grant number: 200021_172538 and 200021_215288), the Swiss Federal Office of Energy (grant number: SI/502135-01), the National Science Foundation Iowa EPSCoR (Grant No 1101284), and the Center for Global and Regional Environmental Research (CGRER), University of Iowa.

References

Ainslie, J.: Calculating the flowfield in the wake of wind turbines, J. Wind Eng. Ind. Aerod., 27, 213–224, https://doi.org/10.1016/0167-6105(88)90037-2, 1988.

Antonia, R., Zhou, Y., and Matsumura, M.: Spectral characteristics of momentum and heat transfer in the turbulent wake of a circular cylinder, Exp. Therm. Fluid Sci., 6, 371–375, https://doi.org/10.1016/0894-1777(93)90015-B, 1993.

Bastankhah, M. and Porté-Agel, F.: Experimental and theoretical study of wind turbine wakes in yawed conditions, J. Fluid Mech., 806, 506–541, https://doi.org/10.1017/jfm.2016.595, 2016.

Bastankhah, M. and Porté-Agel, F.: A New Miniature Wind Turbine for Wind Tunnel Experiments. Part II: Wake Structure and Flow Dynamics, Energies, 10, https://doi.org/10.3390/en10070923, 2017.

Bingöl, F., Mann, J., and Larsen, G. C.: Light detection and ranging measurements of wake dynamics part I: one-dimensional scanning, Wind Energy, 13, 51–61, 2010.

Brugger, P., Debnath, M., Scholbrock, A., Fleming, P., Moriarty, P., Simley, E., Jager, D., Roadman, J., Murphy, M., Zong, H., and Porté-Agel, F.: Lidar measurements of yawed-wind-turbine wakes: characterization and validation of analytical models, Wind Energy Science, 5, 1253–1272, https://doi.org/10.5194/wes-5-1253-2020, 2020.

Brugger, P., Markfort, C., and Porté-Agel, F.: Field measurements of wake meandering at a utility-scale wind turbine with nacelle-mounted Doppler lidars, Wind Energy Science, 7, 185–199, https://doi.org/10.5194/wes-7-185-2022, 2022.

Carbajo Fuertes, F., Markfort, C. D., and Porté-Agel, F.: Wind Turbine Wake Characterization with Nacelle-Mounted Wind Lidars for Analytical Wake Model Validation, Remote Sens.-Basel, 10, https://doi.org/10.3390/rs10050668, 2018.

Cheng, W.-C. and Porté-Agel, F.: A simple physically-based model for wind-turbine wake growth in a turbulent boundary layer, Boundary-Layer Meteorology, 169, 1–10, https://doi.org/10.1007/s10546-018-0366-2, 2018.

Conti, D., Dimitrov, N., Peña, A., and Herges, T.: Probabilistic estimation of the Dynamic Wake Meandering model parameters using SpinnerLidar-derived wake characteristics, Wind Energy Science, 6, 1117–1142, https://doi.org/10.5194/wes-6-1117-2021, 2021.

Crank, J. and Nicolson, P.: A practical method for numerical evaluation of solutions of partial differential equations of the heat-conduction type, Math. Proc. Cambridge, 43, 50–67, https://doi.org/10.1017/S0305004100023197, 1947.

España, G., Aubrun, S., Loyer, S., and Devinant, P.: Wind tunnel study of the wake meandering downstream of a modelled wind turbine as an effect of large scale turbulent eddies, J. Wind Eng. Ind. Aerod., 101, 24 – 33, https://doi.org/10.1016/j.jweia.2011.10.011, 2012.

Keck, R.-E.: Validation of the standalone implementation of the dynamic wake meandering model for power production, Wind Energy, 18, 1579–1591, https://doi.org/10.1002/we.1777, 2015.

Keck, R.-E., Veldkamp, D., Wedel-Heinen, J. J., and Forsberg, J.: A consistent turbulence formulation for the dynamic wake meandering model in the atmospheric boundary layer, Ph.D. thesis, DTU Wind Energy, 2013.

Keck, R.-E., de Maré, M., Churchfield, M. J., Lee, S., Larsen, G., and Aagaard Madsen, H.: On atmospheric stability in the dynamic wake meandering model, Wind Energy, 17, 1689–1710, 2014a.

Keck, R.-E., Mikkelsen, R., Troldborg, N., de Maré, M., and Hansen, K. S.: Synthetic atmospheric turbulence and wind shear in large eddy simulations of wind turbine wakes, Wind Energy, 17, 1247–1267, https://doi.org/10.1002/we.1631, 2014b.

Larsen, G. C., Aagaard Madsen, H., and Bingöl, F.: Dynamic wake meandering modeling, Technical report, Risø National Laboratory, Roskilde, Denmark, 2007.

Larsen, G. C., Madsen, H. A., Thomsen, K., and Larsen, T. J.: Wake meandering: a pragmatic approach, Wind Energy, 11, 377–395, 2008.

Larsen, T. J., Madsen, H. A., Larsen, G. C., and Hansen, K. S.: Validation of the dynamic wake meander model for loads and power production in the Egmond aan Zee wind farm, Wind Energy, 16, 605–624, https://doi.org/10.1002/we.1563, 2013.

Machefaux, E., Larsen, G. C., Troldborg, N., Gaunaa, M., and Rettenmeier, A.: Empirical modeling of single-wake advection and expansion using full-scale pulsed lidar-based measurements, Wind Energy, 18, 2085–2103, https://doi.org/10.1002/we.1805, 2015.

Madsen, H. A., Larsen, G. C., Larsen, T. J., Troldborg, N., and Mikkelsen, R.: Calibration and Validation of the Dynamic Wake Meandering Model for Implementation in an Aeroelastic Code, J. Sol. Energ.-T. ASME, 132, https://doi.org/10.1115/1.4002555, 041014, 2010.

Mann, J.: The spatial structure of neutral atmospheric surface-layer turbulence, Journal of Fluid Mechanics, 273, 141–168, https://doi.org/10.1017/S0022112094001886, 1994.

Medici, D. and Alfredsson, P. H.: Measurements on a wind turbine wake: 3D effects and bluff body vortex shedding, Wind Energy, 9, 219–236, https://doi.org/10.1002/we.156, 2006.

Mehta, D., van Zuijlen, A., Koren, B., Holierhoek, J., and Bijl, H.: Large Eddy Simulation of wind farm aerodynamics: A review, J. Wind Eng. Ind. Aerod., 133, 1–17, https://doi.org/10.1016/j.jweia.2014.07.002, 2014.

Moeng, C.-H. and Sullivan, P. P.: A Comparison of Shear- and Buoyancy-Driven Planetary Boundary Layer Flows, Journal of Atmospheric Sciences, 51, 999 – 1022, https://doi.org/10.1175/1520-0469(1994)051<0999:ACOSAB>2.0.CO;2, 1994.

Pearson, G., Davies, F., and Collier, C.: An analysis of the performance of the UFAM pulsed Doppler lidar for observing the boundary layer, J. Atmos. Ocean Tech., 26, 240–250, https://doi.org/10.1175/2008JTECHA1128.1, 2009.

Qian, G.-W. and Ishihara, T.: A New Analytical Wake Model for Yawed Wind Turbines, Energies, 11, https://doi.org/10.3390/en11030665, 2018.

Reinwardt, I., Gerke, N., Dalhoff, P., Steudel, D., and Moser, W.: Validation of wind turbine wake models with focus on the dynamic wake meandering model, J Phys. Conf. Ser., 1037, 072 028, https://doi.org/10.1088/1742-6596/1037/7/072028, 2018.

Reinwardt, I., Schilling, L., Dalhoff, P., Steudel, D., and Breuer, M.: Dynamic wake meandering model calibration using nacelle-mounted lidar systems, Wind Energy Science, 5, 775–792, https://doi.org/10.5194/wes-5-775-2020, 2020.

Reynolds, A.: The variation of turbulent Prandtl and Schmidt numbers in wakes and jets, Int. J. Heat Mass Tran., 19, 757–764, https://doi.org/10.1016/0017-9310(76)90128-9, 1976.

Taylor, G., Milborrow, D., McIntosh, D., and Swift-Hook, D.: Wake measurements on the Nibe windmills, in: Proceedings of Seventh BWEA Wind Energy Conference, Oxford, pp. 67–73, 1985.

Taylor, G. I.: Diffusion by continuous movements, P Lond. Math. Soc., 2, 196–212, 1922.

Taylor, G. I.: The spectrum of turbulence, P. Roy. Soc. Lond. A. Mat., 164, 476–490, 1938.

Thøgersen, E., Tranberg, B., Herp, J., and Greiner, M.: Statistical meandering wake model and its application to yaw-angle optimisation of wind farms, in: J Phys. Conf. Ser., vol. 854, p. 012017, IOP Publishing, 2017.

Trujillo, J.-J., Bingöl, F., Larsen, G. C., Mann, J., and Kühn, M.: Light detection and ranging measurements of wake dynamics. Part II: two-dimensional scanning, Wind Energy, 14, 61–75, 2011.